Supporting information for

Structural frustration, metastability and cascade of polar phases in a layered lead bromide perovskite

Mirosław Mączka,[*,a] Katarzyna Fedoruk-Piskorska,[*,b,c] Anna Gągor,[a] Jan K. Zaręba,[d] Dagmara Stefańska,[a] Maciej Ptak,[a] Dawid Drozdowski,[a] and Adam Sieradzki[b]

[a]*Institute of Low Temperature and Structure Research, Polish Academy of Sciences, 50-422 Wrocław, Poland*

[b]*Institute of Physics, University of Silesia, Uniwersytecka 4, 40-007 Katowice, Poland*

[c]*Department of Experimental Physics, Wrocław University of Science and Technology, Wrocław, Poland*

[d]*Institute of Advanced Materials, Faculty of Chemistry, Wrocław University of Science and Technology, 50-370 Wrocław, Poland*

e-mail: m.maczka@intibs.pl; katarzyna.fedoruk-piskorska@pwr.edu.pl

Table S1. Selected hydrogen-bond parameters of CPA_2PbBr_4.

D*—H···*A	***D*—H (Å)**	**H···*A* (Å)**	***D*···*A* (Å)**	***D*—H···*A* (°)**
II, 350 K				
N5—H5A···Br1^{i}	0.89	2.56	3.430 (17)	164.7
N5—H5B···Br1^{ii}	0.89	2.56	3.382 (17)	153.2
N5—H5C···Br2^{ii}	0.89	2.77	3.526 (17)	144.1
III, 295 K				
N1—H1A···Br3	0.89	2.59	3.366 (14)	146.0
N1—H1B···Br3^{iv}	0.89	2.54	3.361 (15)	153.2
N1—H1C···Br1	0.89	2.74	3.498 (17)	143.7
IV, 100 K				
N9—H9A···Br8^{v}	0.91	2.48	3.385 (11)	177.4
N9—H9B···Br5^{v}	0.91	2.84	3.413 (12)	122.3
N9—H9B···Br1	0.91	2.69	3.429 (12)	138.9
N9—H9C···Br4	0.91	2.44	3.341 (12)	169.5
N5—H5A···Br3	0.91	2.48	3.390 (10)	174.5
N5—H5B···Br2	0.91	2.77	3.407 (12)	127.6
N5—H5B···Br6	0.91	2.76	3.446 (12)	133.2
N5—H5C···Br7	0.91	2.44	3.348 (12)	174.6
N13—H13A···Br2	0.91	2.82	3.489 (13)	131.6
N13—H13A···Br6	0.91	2.82	3.469 (12)	129.2
N13—H13B···Br4	0.91	2.45	3.329 (11)	162.9
N13—H13C···Br8	0.91	2.50	3.407 (13)	171.1
N1—H1A···Br5^{v}	0.91	2.76	3.474 (13)	136.6
N1—H1A···Br1	0.91	2.88	3.496 (12)	126.0
N1—H1B···Br7^{v}	0.91	2.45	3.325 (11)	161.8
N1—H1C···Br3	0.91	2.49	3.388 (13)	170.1
V, 100 K				
N1—H1A···Br4^{vi}	0.91	2.64	3.33 (6)	132.8
N1—H1B···Br3^{vii}	0.91	2.53	3.30 (4)	142.6
N1—H1C···Br1	0.91	2.85	3.48 (6)	127.7
N5—H5A···Br4	0.91	2.57	3.39 (5)	150.0
N5—H5B···Br3^{viii}	0.91	2.42	3.33 (7)	175.9
N5—H5C···Br2^{vi}	0.91	2.56	3.45 (6)	167.6

Symmetry code(s): (i) -*x*+1/2, -*y*+1, *z*-1/2; (ii) -*x*+1/2, *y*+1/2, *z*; (iii) *x*-1/2, -*y*+1/2, -*z*+1; (iv) *x*, -*y*+1, *z*+1/2; (v) *x*, *y*, *z*-1; (vi) -*x*+1, *y*+1/2, -*z*+1; (vii) *x*, *y*, *z*+1; (viii) -*x*+1, *y*-1/2, -*z*+1.

Table S2. Comparison of structural and optical parameters for various phases of CPA_2PbBr_4.

phase	Pb-Br-Pb angle (θ_{tilt}, °)	D_{in}/ D_{out}	$\Delta d \cdot 10^{-3}$	σ^2 (°)	Exciton nm (eV)	E_g (eV)	PL nm (eV)
I, *Cmca* (370 K)	153.7	26.3/0	5.1	0			
II, *Pbca* (350 K)	153.7	26.1/3.1	3.3	6			
III, *Cmc2₁* (295 K)	158.8 145.5	24.2/0 34.5/0	9.8	18	401(3.09)	3.15	401.4 (3.09) 426.6 (2.91) 488 (2.54)
IV, *Pna*2_1 (100 K)	157.1 157.0 138.2 138.3	22.8/2.0 22.9/2.4 40.6/9.6 41.4/6.4	16.2 11.9	34 32			386.1 (3.21) 389.9 (3.18) 397.6 (3,12) 583 (2.13)
V, *P*2_1 (100 K)	144.7 146.9	29.6/20.2 26.8/18.2	6.9	15			388.9 (3.19) 398.0 (3.12) 592 (2.09)

Table S3. Raman wavenumbers (in cm^{-1}) of CPA_2PbBr_4 in the heating run at 80, 190, 250, 350 and 370 K together with the proposed assignment.[a] For the comparison sake, Raman wavenumbers obtained in the cooling run at 80 K are present in the last column on the right.

370 K (*Cmce* phase)	350 K (*Pbca* phase)	250 K (*Cmc2₁* phase)	190 K (*P2₁* phase)	80 K (*Pna2₁* phase)	80 K (*P2₁* phase)	assignment
3178w,b	3181w,b	3189m	3189vw+3182vw	3194m+3184w	3184vw	$\nu_{as}(NH_3^+)$
			3154w	3161vw+3153w	3154w	
		3131w	3120m	3135w+3130w	3120m	$\nu_{as}(NH_3^+)$
				3069vw+3054vw		overtones
3062vb,m	3053vb,s	3036s	3079m+3057sh	3041sh+3030vs	3077s	$\nu_s(NH_3^+)$
3007sh	3007w	3008m	3013s	3006m+3003sh	3013s	$\nu_{as}(CH_2)$
2996m	2994m	2995m	2996vw	2995s	2996w	$\nu_{as}(CH_2)$
2966s	2966s	2967s	2966sh+2964s	2978m+2961m	2967m+2964m	$\nu_s(CH_2)$
2943s	2942s	2945s	2944m	2947m+2938s	2944m	$\nu_s(CH_2)$
2920s	2920s	2928m	2918s	2929sh	2918m	$\nu_s(CH_2)$
2911sh	2910sh	2911s	2910s	2915m+2902m	2910s	$\nu_s(CH_2)$
2876w	2876w	2877w	2879w+2876w	2886sh+2878w	2880w	overtone
1588m	1585m	1594w		1600w+1594w		$\delta_{as}(NH_3)$
1575m	1570w	1577w+1569w	1578s	1578w+1568w	1579s	$\delta_{as}(NH_3)$
1484m	1488s	1493s	1473sh+1470s	1493s+1487w	1473sh+1471s	$\delta_s(NH_3)$
1442w	1449w	1452w		1463w+1460w		$\delta(CH_2)$
		1446vw	1451w	1453vw+1449vw	1452w	$\delta(CH_2)$
1427vw	1431vw	1429w	1439w+1428w	1433w+1423w	1440w+1429m	$\delta(CH_2)$
1395vw	1398w	1398w	1398w	1402sh+1399w	1398w	$\omega(CH_2)$
	1337w	1337w	1337m	1336vw	1337m	$\omega(CH_2)$
1323w	1324m	1325s	1329m	1329s	1329m	$\omega(CH_2)$
	1302w	1302w	1311w+1303m	1303w	1315w+1303m	$\omega(CH_2)$
	1262w	1263w	1269m	1263vw	1270s	$\tau(CH_2)$
1214vw	1215w	1217m	1222s	1218m	1223s	$\tau(CH_2)$
		1134w		1137m		$\rho(NH_3^+)$
1120vw	1122w	1124m	1127s	1127m	1128s	$\rho(CH_2)$

	1094vw	1096w	1101w	1100vw+1095vw	1102w	$\rho(CH_2)$
	1050w	1051m		1052m		$\nu(CN)$
1041vw	1040w	1040w	1043m	1039w	1044m	$\rho(CH_2)$
998vw	998w	1001w	1001w	1008w	1002w	$\nu_{as}(CCC)$
	989w	991w		995vw		$\rho(CH_2)$
961vw	966w	969w	973m	973w	973m	$\omega(NH,CH)$
934vw	936s	938s	939vw+929m	940s+930w	939vw+930m	$\nu_s(CCC)$
834vw	836w	839w	841m	843sh+840w	842m	$\rho(CH_2)$
777w	777w	779w+772w	779m	768w	780s	$\rho(CH_2)$
738vw	739w	740w	741vw	741w		$\nu(CCl)$
659m	660m	660m	656s	660w	657s	$\nu(CCl)$
483vw	483m	484m	485s	487m	486s	$\delta(CCN)$
	424w	425w		425w		$\delta(CCC)$
	333vw	335w	337w	330w+326sh	339m	$\delta(CCCl)$
294m,b	290m,b	288w,b	307s	286w,b	307s	$\tau(NH_3^+)$
		266w	270w		271w	$\tau(CH_3)$
		188sh	171m	191m	175m	L+ T'+ Pb-Br stretch
145sh	146sh	143m	152m	156m	158m	L+ T'+ Pb-Br stretch
116m	116m	118s	117m+109w	121vs+113w	123m	L+ T'+ Pb-Br stretch
		88sh		94s+92s		Pb-Br bend
72vs	76vs	82vs	82vs+71m	86s+78s+73m+71m	84vs+73s	Pb-Br bend
56vs	58vs	60vs+54sh	66m+64sh+55m	62vs+52vs	68w+57s	Pb-Br bend
35vs+22sh	33vs+22sh	39vs+30sh	40sh+36vs	41vs+33s+21s	42vs+37vs	$L(PbBr_6)$

[a] key: vs, very strong; s, strong; m, medium; w, weak; vw, very weak; sh, shoulder; ν, stretching; δ, bending (scissoring); ρ, rocking; ω, wagging; τ, twist; L, librational mode of organic cation; T', translational mode of organic cation.

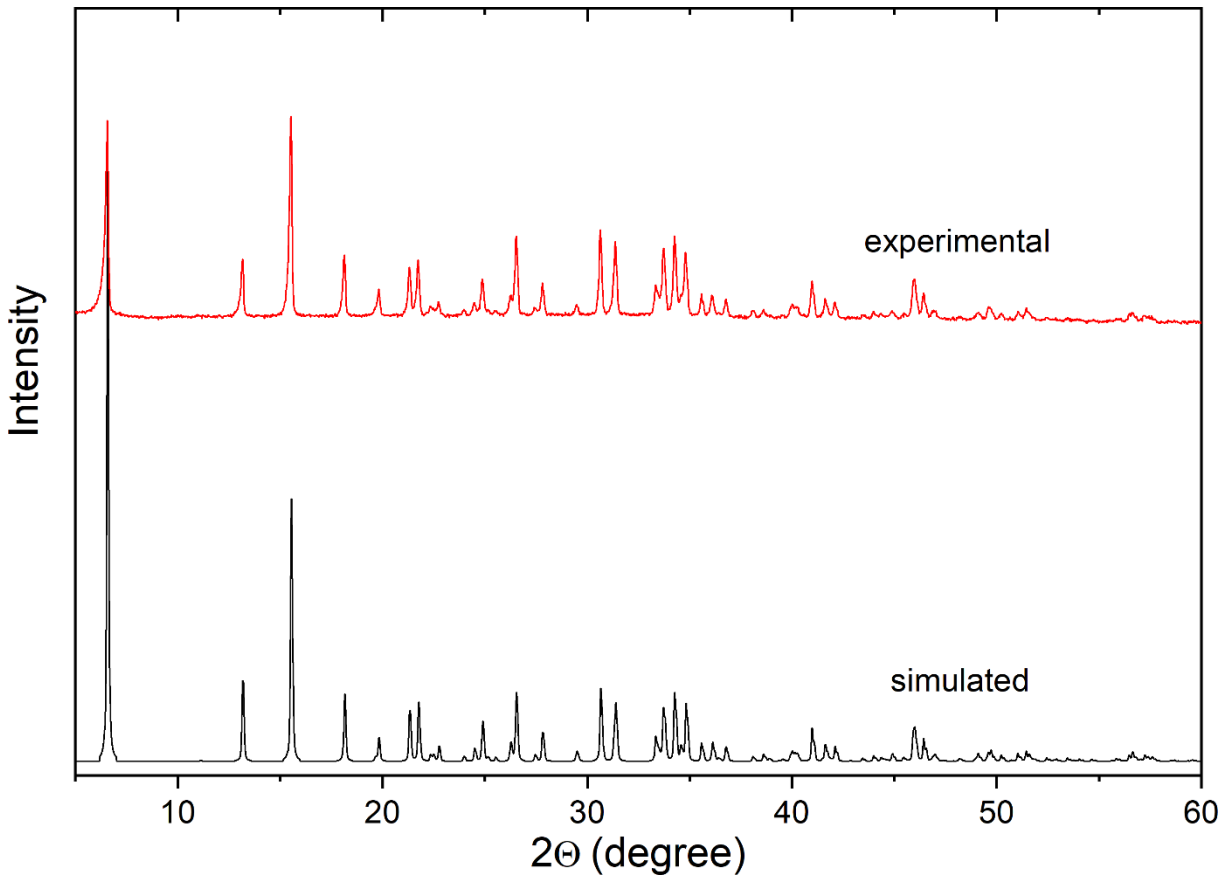

Figure S1. Experimental and calculated PXRD patterns of pristine CPA_2PbBr_4.

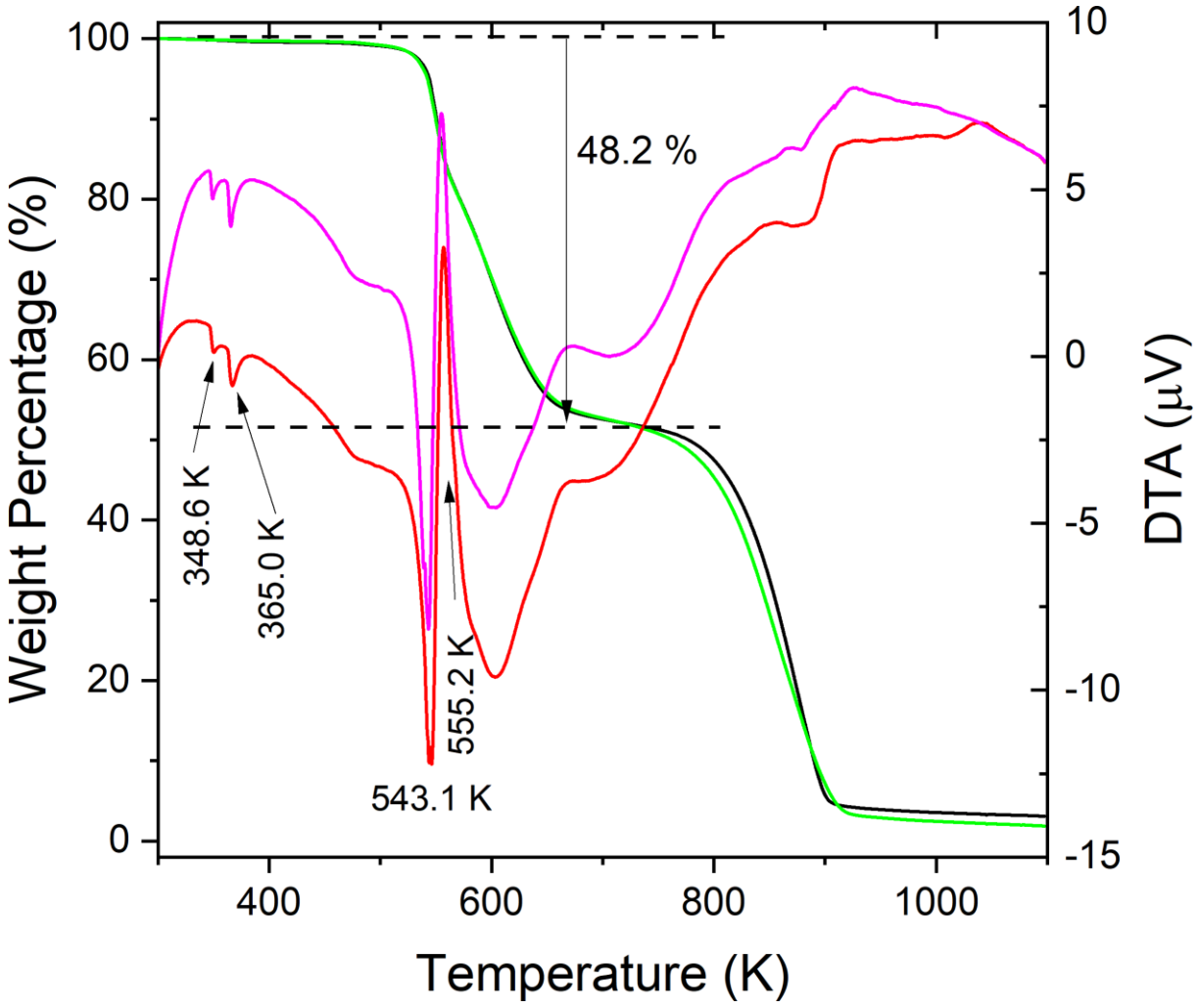

Figure S2. TG (solid black line) and DTA (red line) plots of pristine CPA_2PbBr_4. Green and magenta lines correspond to TG and DTA of CPA_2PbBr_4 annealed at 380 K for 10 minutes.

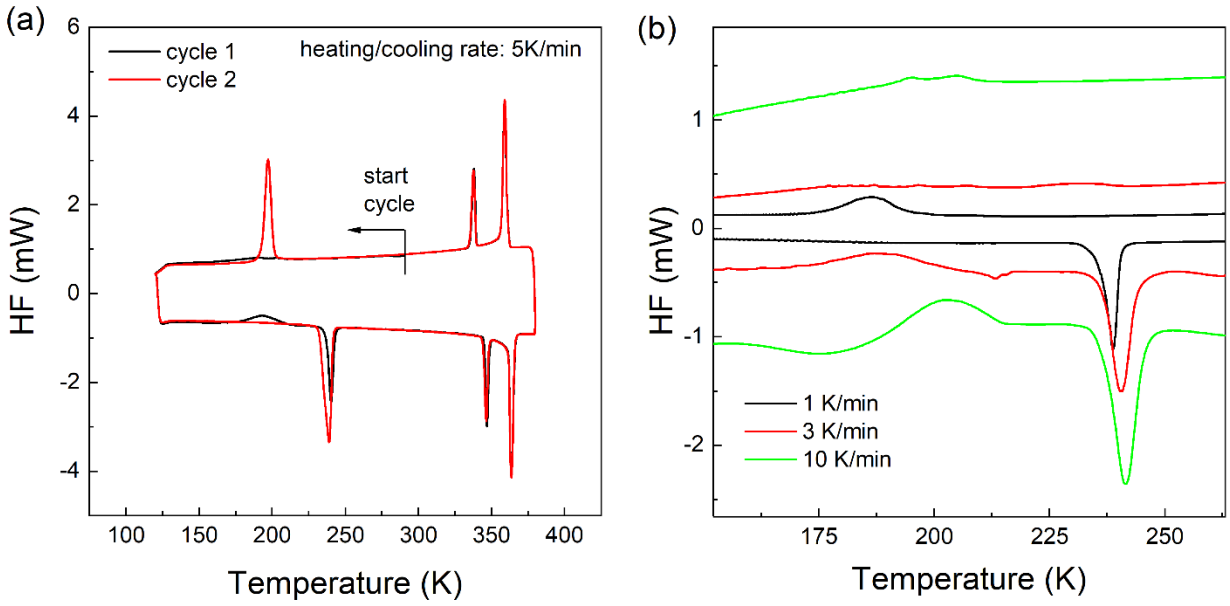

Figure S3. (a) DSC traces of CPA_2PbBr_4 measured at 5 K/min rate (first loop, black line: 288K→120 K→380 K→300 K; second loop, red line: 300 K→120 K→380 K→300 K). (b) DSC curves of CPA_2PbBr_4 recorded during the first thermal cycle at different heating/cooling rates (1, 3, and 10 K/min).

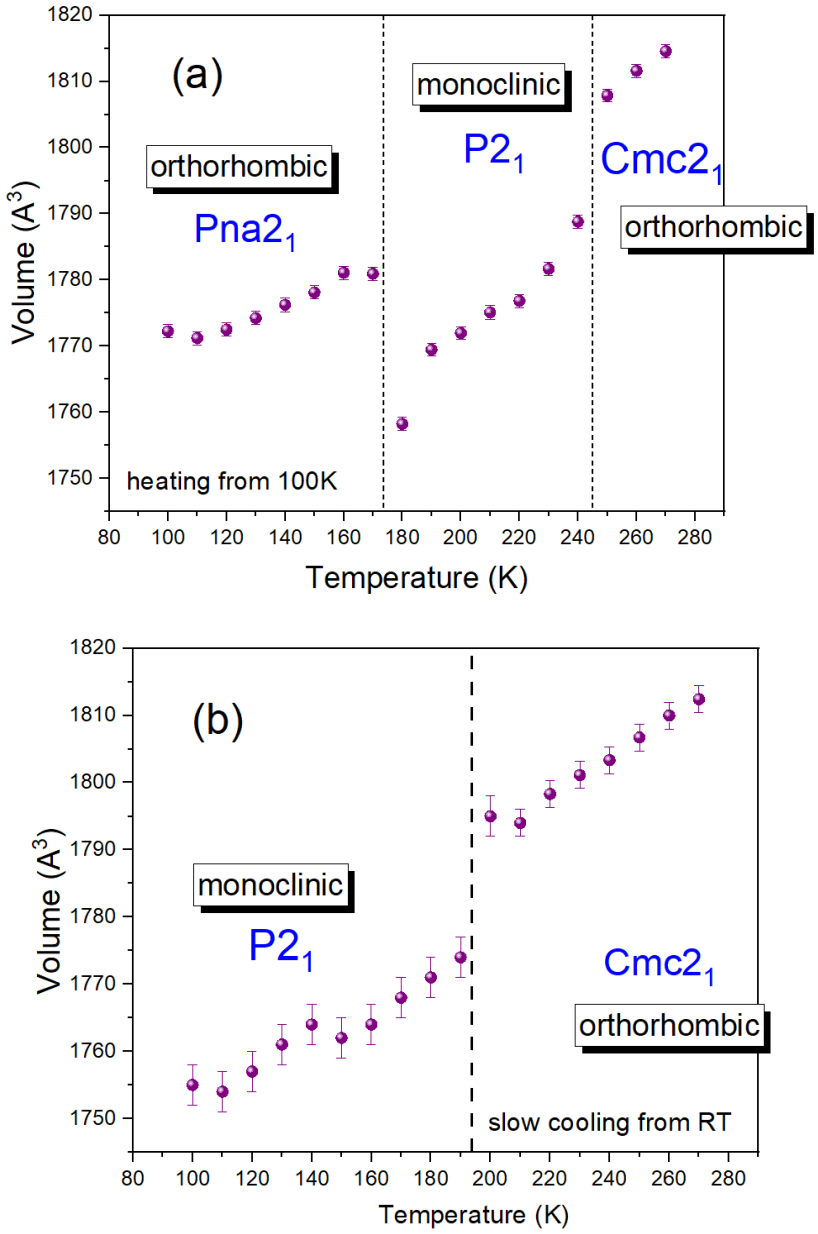

Figure S4. The unit cell volume changes with temperature. (a) pristine sample quenched to 100 K at rate ~5 K/min and then gradually heated (2.5 K/min between the temperature points and 30 min. stabilization at each point for data collection); (b) pristine sample gradually cooled from RT down to 100 K (2.5 K/min between the temperature points and 30 min. stabilization at each point).

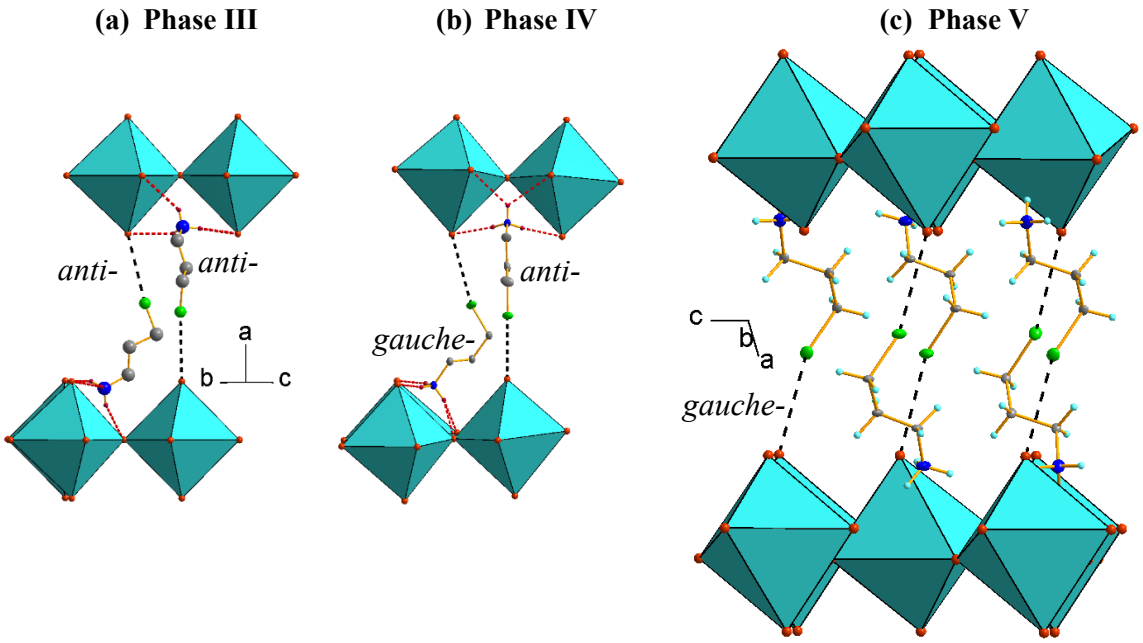

Figure S5. The *anti* and *gauche* conformations of CPA^+ in III (a) and IV phase (b); the view along polar direction in monoclinic phase V (c). All CPA^+ in V adopt *gauche* conformation; dashed black lines stand for halogen-halogen interactions, red for HBs.

Supplementary discussion – Raman spectroscopy

Detailed inspection of the metastable phase **IV** spectra reveals specific splitting patterns associated with cation conformation. Since phase **IV** contains two independent CPA^+ cations in *anti* conformation and two in *gauche* conformation, internal modes should theoretically split into four components (two doublets). However, Figure S6 and Table S3 show that most modes exhibit splitting into only two resolvable components. This suggests that the two *anti* conformers possess sufficiently similar structural environments that their vibrational energies are nearly degenerate and cannot be resolved given the significant thermal broadening. A similar degeneracy likely applies to the *gauche* conformers.

The structural relationship between the HT phase **III** and the LT metastable phase **IV** is further illuminated by specific spectral markers (Figure S7). Beyond the broadness of the $\tau(NH_3)$ band, the similarity in the $\nu_s(NH_3)$ mode positions, i.e. 3033 cm^{-1} in phase **IV** (170 K) versus 3036 cm^{-1} in phase **III** (250 K) corroborates X-ray evidence that the cationic sub-lattice adopts a similar averaged orientation in both phases. However, the disorder in phase **III** is quantitatively higher, as evidenced by the larger FWHM of the $\tau(NH_3)$ band (71.8 cm^{-1} vs 58.1 cm^{-1}) and the disappearance of mode splitting observed in phase **IV**. The reduction in the number of Raman bands in phase **III** aligns with the crystallographic reduction in independent cation and halide sites.

Furthermore, closer monitoring of the lattice region during the **IV** → **V** transition (Figure S6) reveals that residual bands characteristic of phase **IV** persist up to 180 K before disappearing completely at 190 K. This co-existence interval highlights the kinetic barrier associated with the reorganization of the octahedral framework. In the high-temperature regime, the transition from phase **II** to **I** is spectrally subtle; while the internal modes remain static, the continuous increase in bandwidths across the entire spectral range confirms that the **II** →**I** transition is driven by dynamic orientational disordering rather than displacive structural modification.

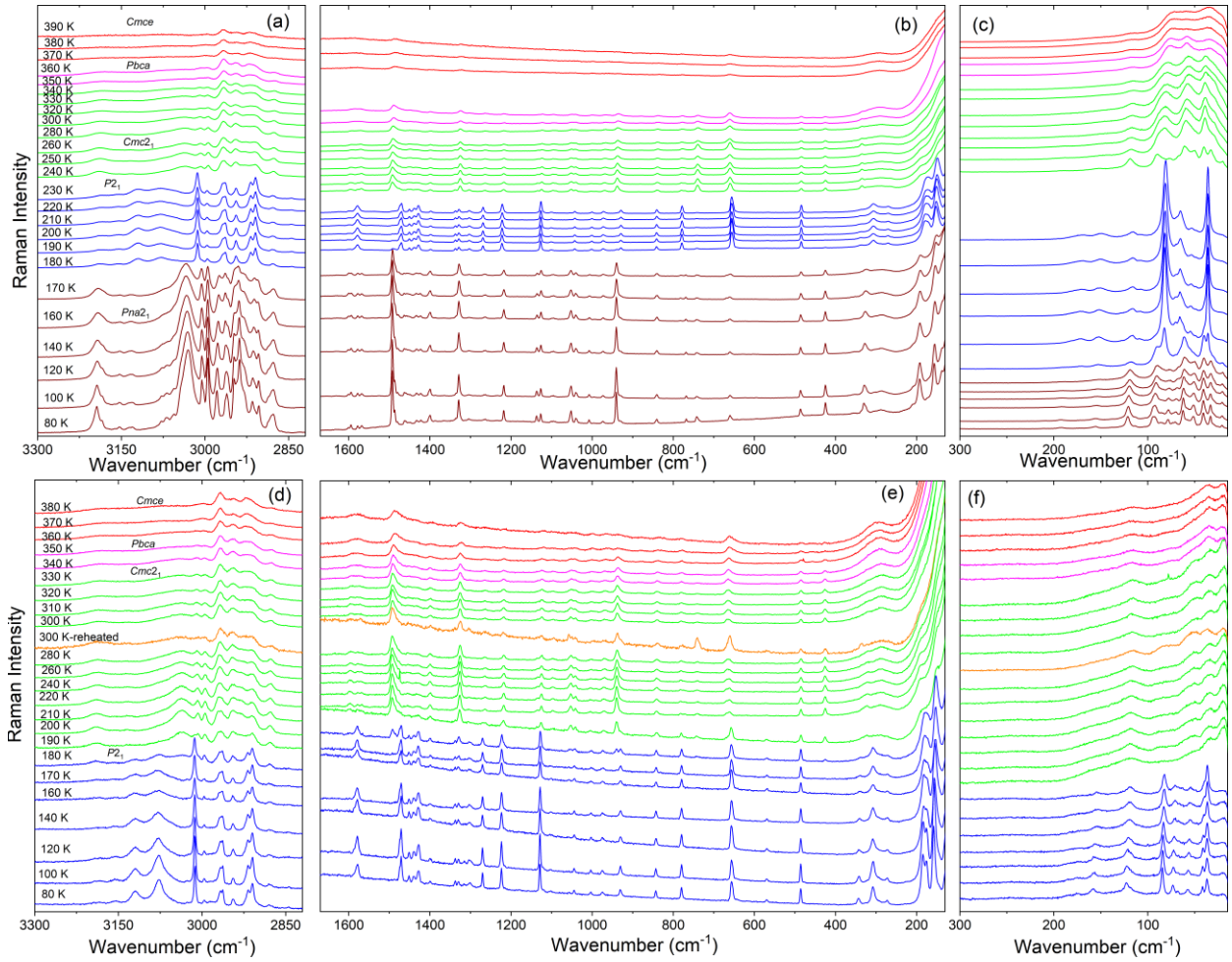

Figure S6. Raman spectra of CPA_2PbBr_4 during heating (a,b,c) and cooling (d,e,f) runs in the (a,d) 3300-2820 cm^{-1}, (b,e) 1670-130 cm^{-1} and (c,f) 300-15 cm^{-1} range.

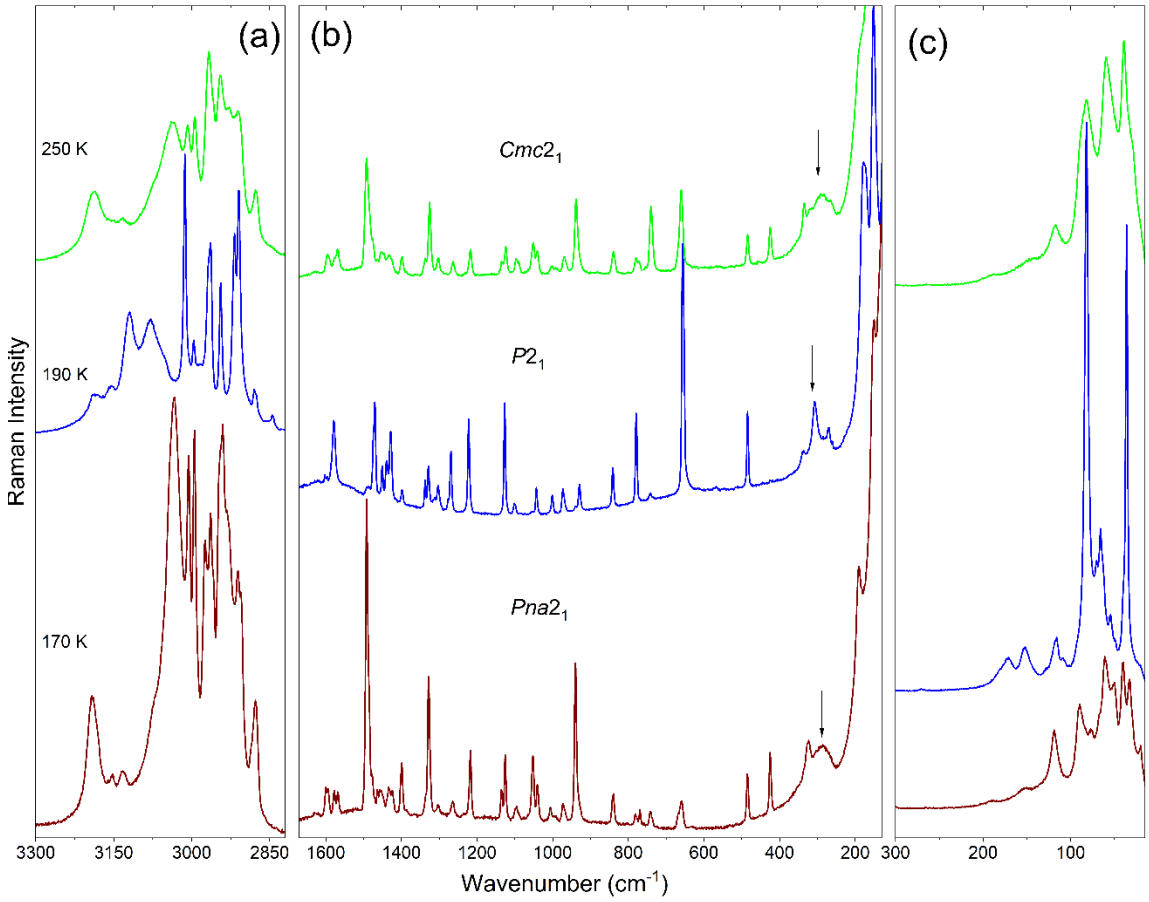

Figure S7. Raman spectra of CPA_2PbBr_4 recorded at 170, 190 and 250 K during heating run in the (a) 3300-2820 cm^{-1}, (b) 1670-130 cm^{-1} and (c) 300-15 cm^{-1} range. Arrows indicate the $\tau(NH_3^+)$ band, which exhibits pronounced narrowing in the $P2_1$ phase.

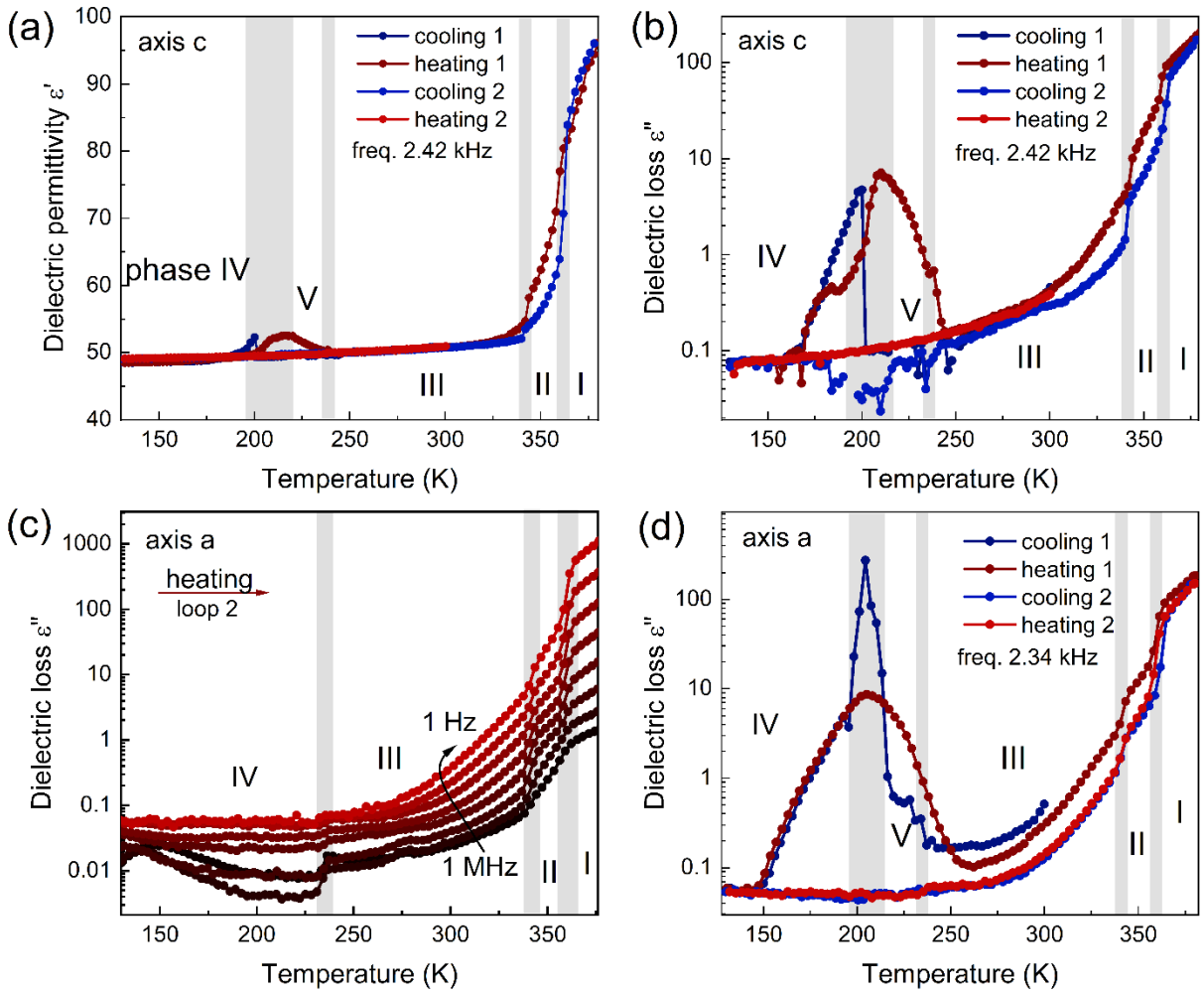

Figure S8. Temperature dependence of dielectric properties of single crystals measured along the crystallographic axes. (a) Real part of dielectric permittivity (ε′) and (b) dielectric loss (ε″) measured along the c-axis at ~2.42 kHz. (c) Dielectric loss (ε″) along the a-axis at different frequencies. (d) Dielectric loss (ε″) along the a-axis at ~2.34 kHz.

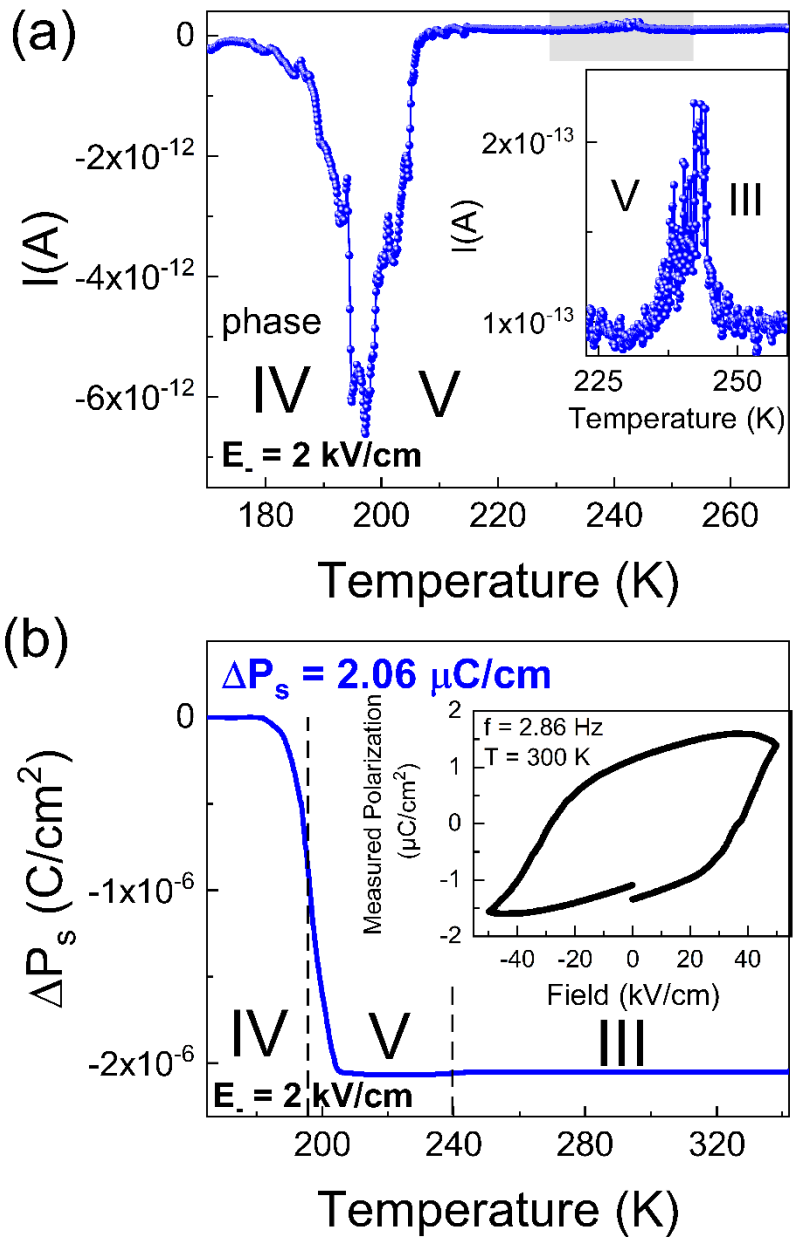

Figure S9. (a) Changes of the pyroelectric current of a single crystal in the direction of the polar axis after negative poling in a DC electric field. (b) Relative change of spontaneous polarization as a function of temperature determined by the integration of the pyroelectric current. Inset P-E hysteresis loop measured at 300 K.

Supplementary discussion – linear optical properties:

The optical properties of CPA_2PbBr_4 present interesting contrasts when compared to its structural analogues. While the excitonic absorption position (401 nm) is nearly identical to that of BA_2PbBr_4 BA= butylammonium, excitonic peak at 404 nm)[1] and BZA_2PbBr_4 (BZA=benzylammonium, excitonic peak at 400 nm)[2], the behavior of the self-trapped exciton (STE) emission reveals the subtle influence of the halide substitution in the organic cation. For the chloride analogue, CPA_2PbCl_4, the STE emission at 80 K is centered at 598 nm, resulting in a significantly larger Stokes shift of ~280 nm compared to the ~195 nm observed for CPA_2PbBr_4. Since both compounds exhibit comparable magnitudes of octahedral tilting (out-of-plane tilt D_{out}=8.2° for the chloride[3] vs 9.6° for phase **IV** of the bromide), the variation in Stokes shift cannot be attributed solely to structural distortion. Instead, it points to differences in electron-phonon coupling strength,[1,4] likely governed by the distinct phonon energies of the inorganic lattice upon substituting Cl with Br.

Detailed analysis of the PL quenching dynamics provides further insight into the trap states. While the main text discusses heating parameters, the cooling run yields slightly different activation energies due to the hysteresis of the PTs. In the HT phase **III**, the quenching of the Near-Bandgap Emission (NBE) during cooling yields an activation energy E_a of 225 meV (Figure S15), comparable to the heating value. However, the STE quenching in phase **III** during cooling shows an E_a of 173 meV. Notably, in the LT regime of phase **V** (below 190 K upon cooling), the STE quenching activation energy remains low at approximately 51 meV (Figure S16). This value is nearly identical to that observed in the metastable phase **IV** during heating, suggesting that despite their structural differences, the depth of the self-trapping potential or the phonon modes coupling to the exciton are similar in both low-temperature polymorphs.

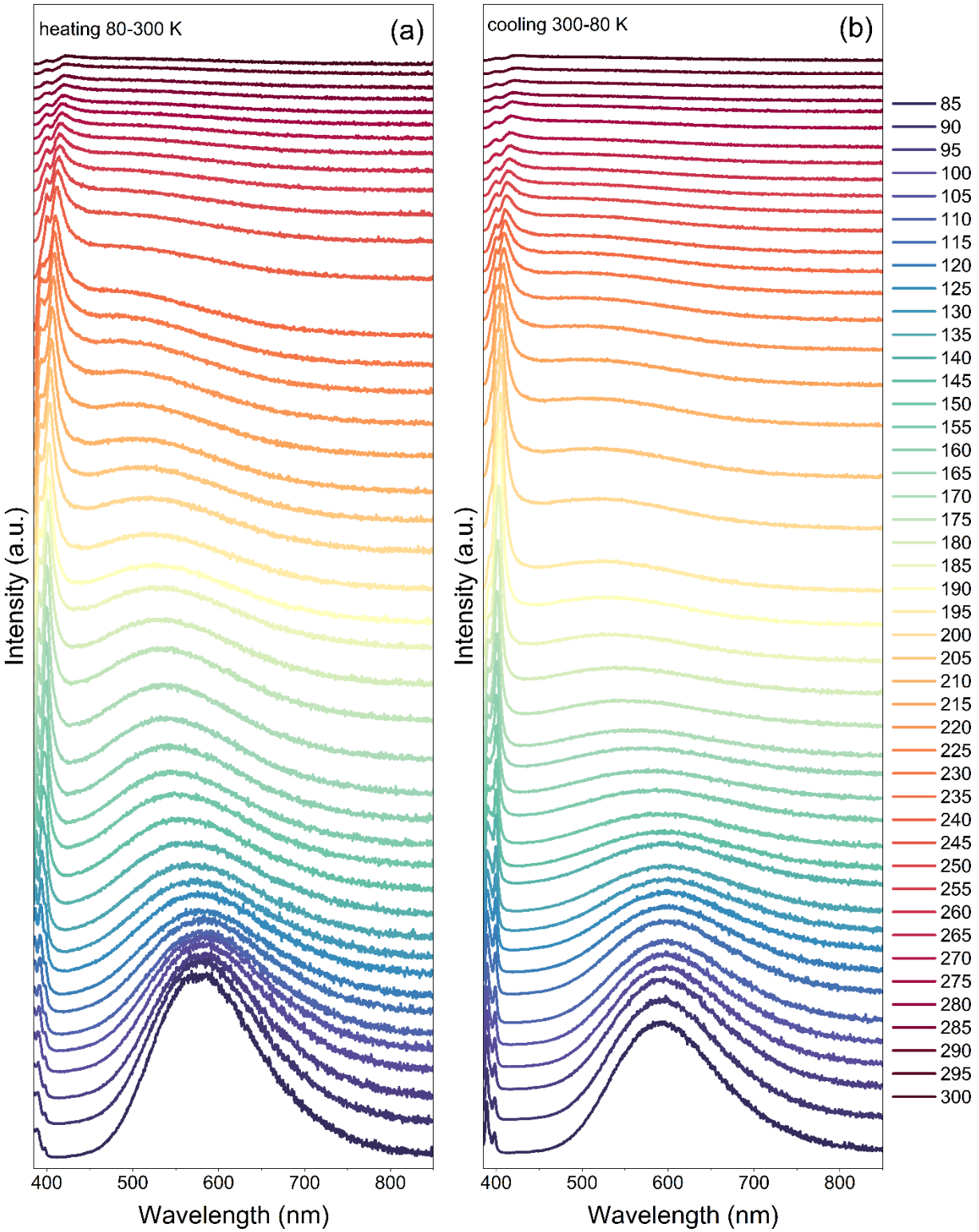

Figure S10. Emission spectra of CPA_2PbBr_4 in the 385-850 nm range measured during (a) heating from 85 to 300K and (b) cooling from 300 to 85 K.

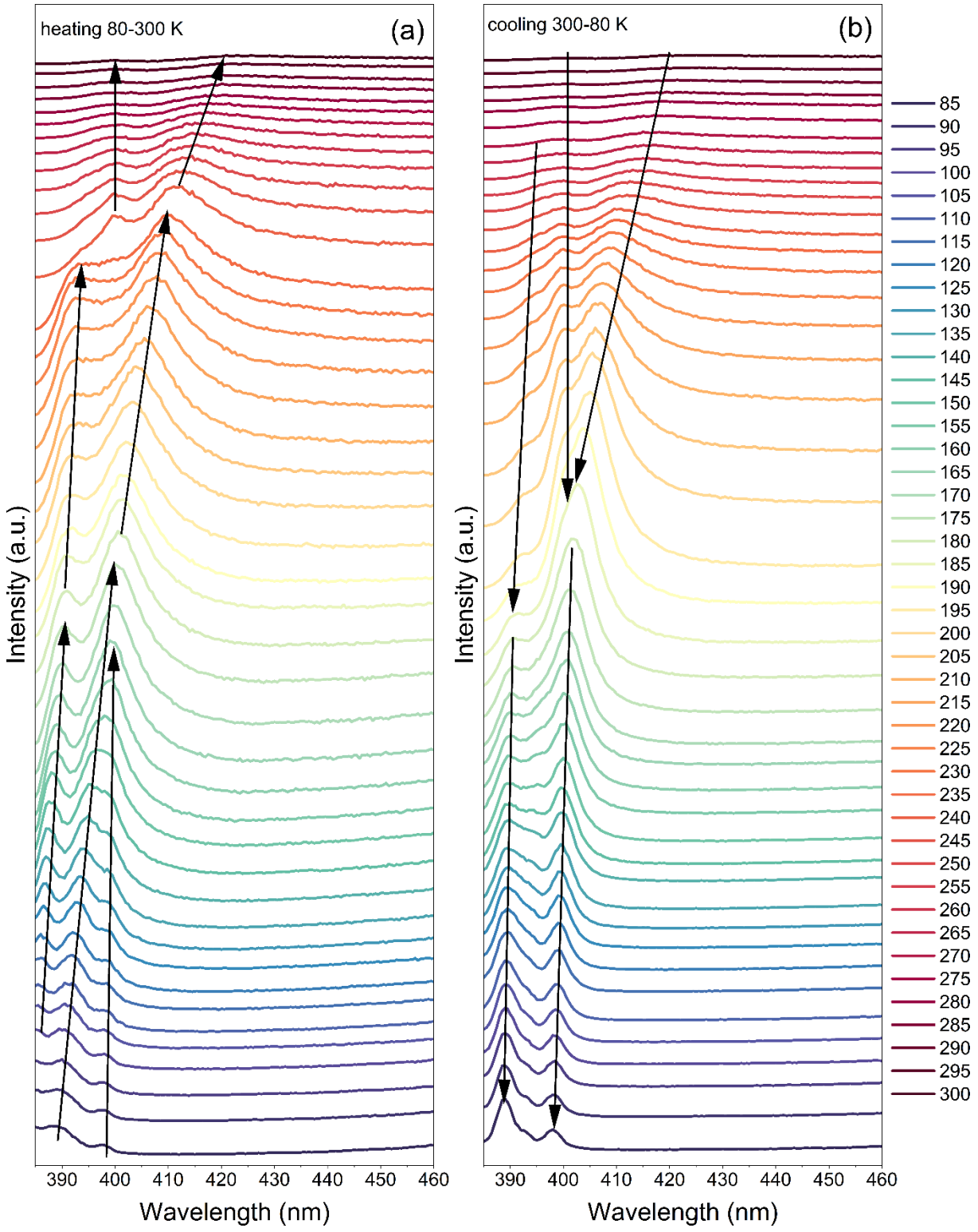

Figure S11. Emission spectra of CPA_2PbBr_4 in the 385-460 nm range measured during (a) heating from 85 to 300K and (b) cooling from 300 to 85 K.

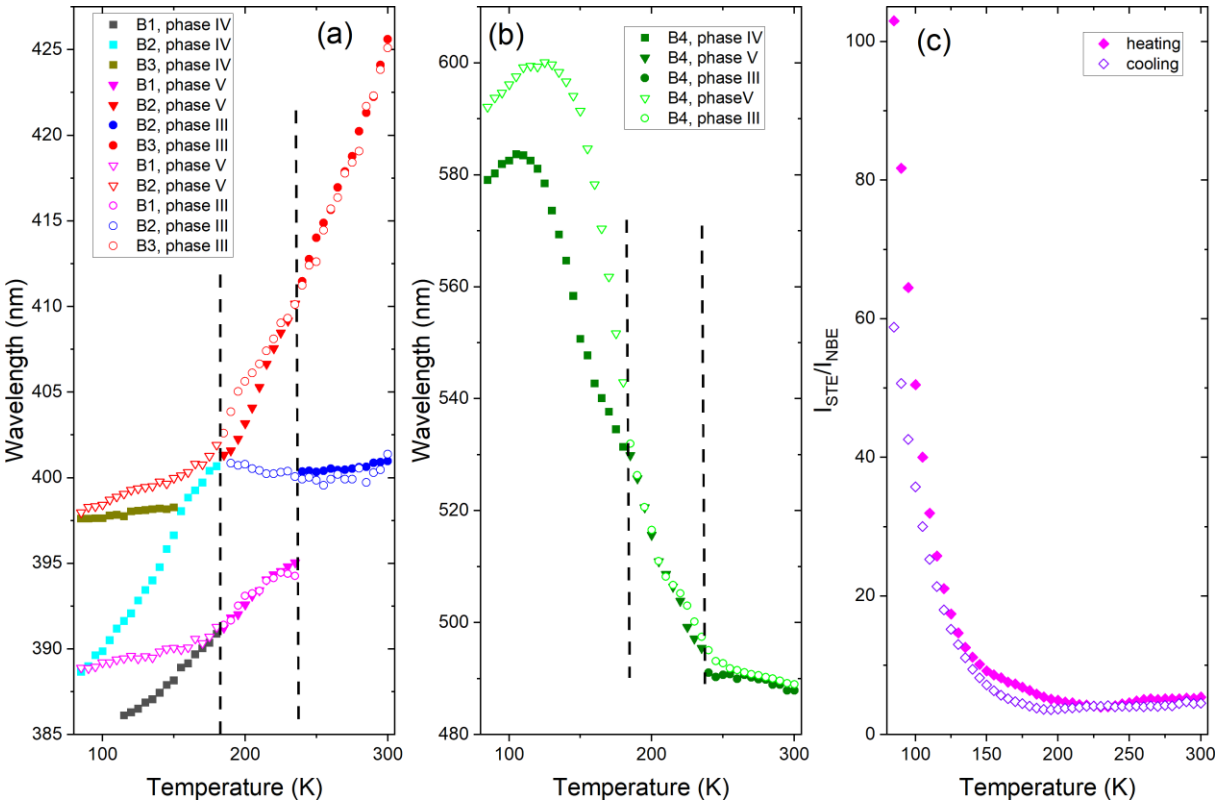

Figure S12. Changes of maximum peaks' position with temperature for the (a) NBE and (b) STE bands and the sample heated from 85 to 300 K (closed symbols) and cooled from 300 to 85 K (open symbols).Vertical lines indicate the phase transition temperatures during heating; squares, down triangles nd circles correspond to phase IV, V and III, respectively. (c) temperature dependence of intensity ratio between STE and NBE bands.

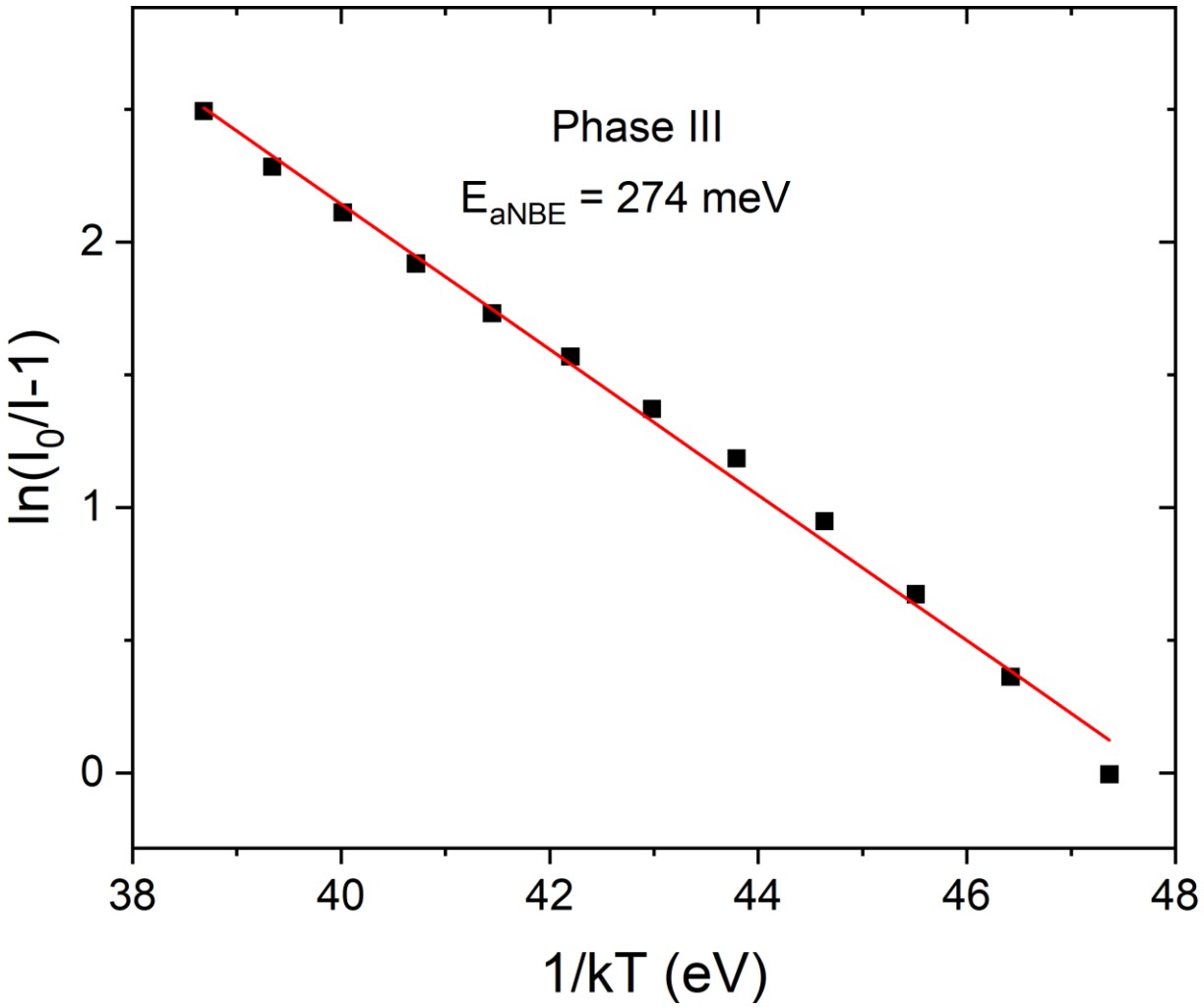

Figure S13. Logarithm of I_0/I-1 as a function of 1/kT of NBE PL of CPA_2PbBr_4 during heating from 85 to 300 K. E_a was extracted by fitting the Arrhenius equation.

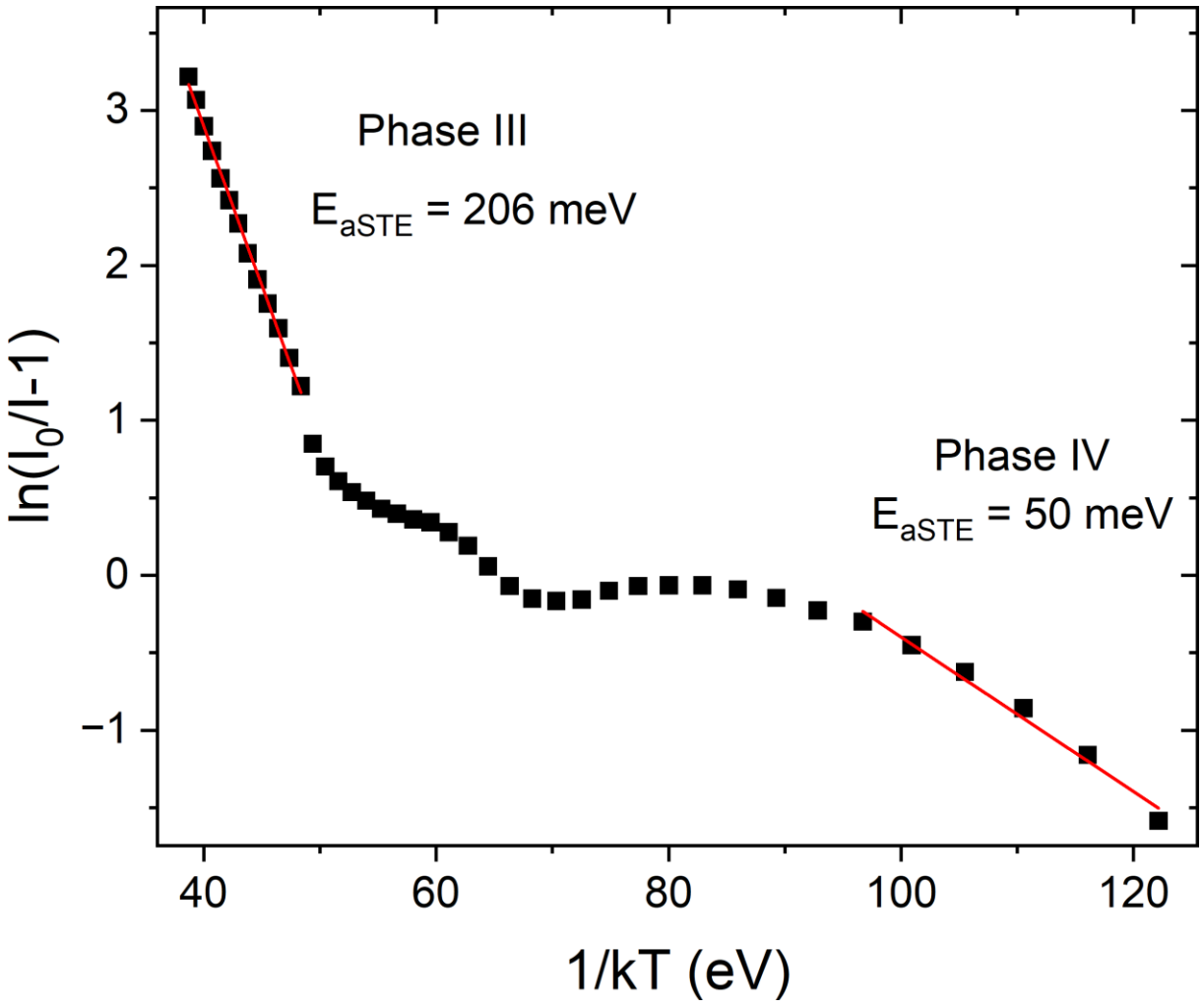

Figure S14. Logarithm of I_0/I-1 as a function of 1/kT of STE PL of CPA_2PbBr_4 during heating from 85 to 300 K. E_a was extracted by fitting the Arrhenius equation.

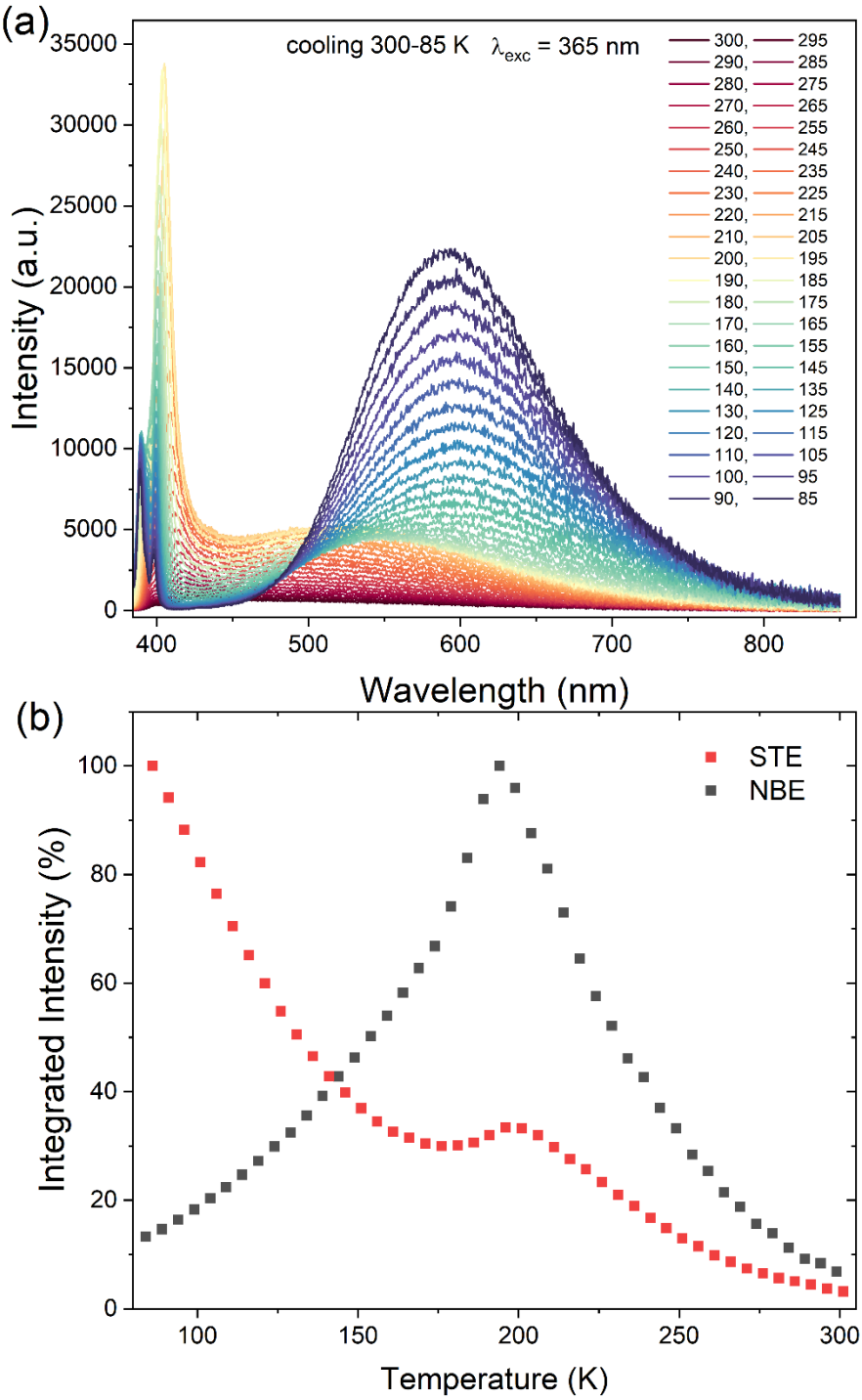

Figure S15. (a) PL spectra of CPA_2PbBr_4 during cooling from 300 to 85 K. (b) Temperature dependence of integrated intensity of STE and NBE emission bands of CPA_2PbBr_4 during cooling.

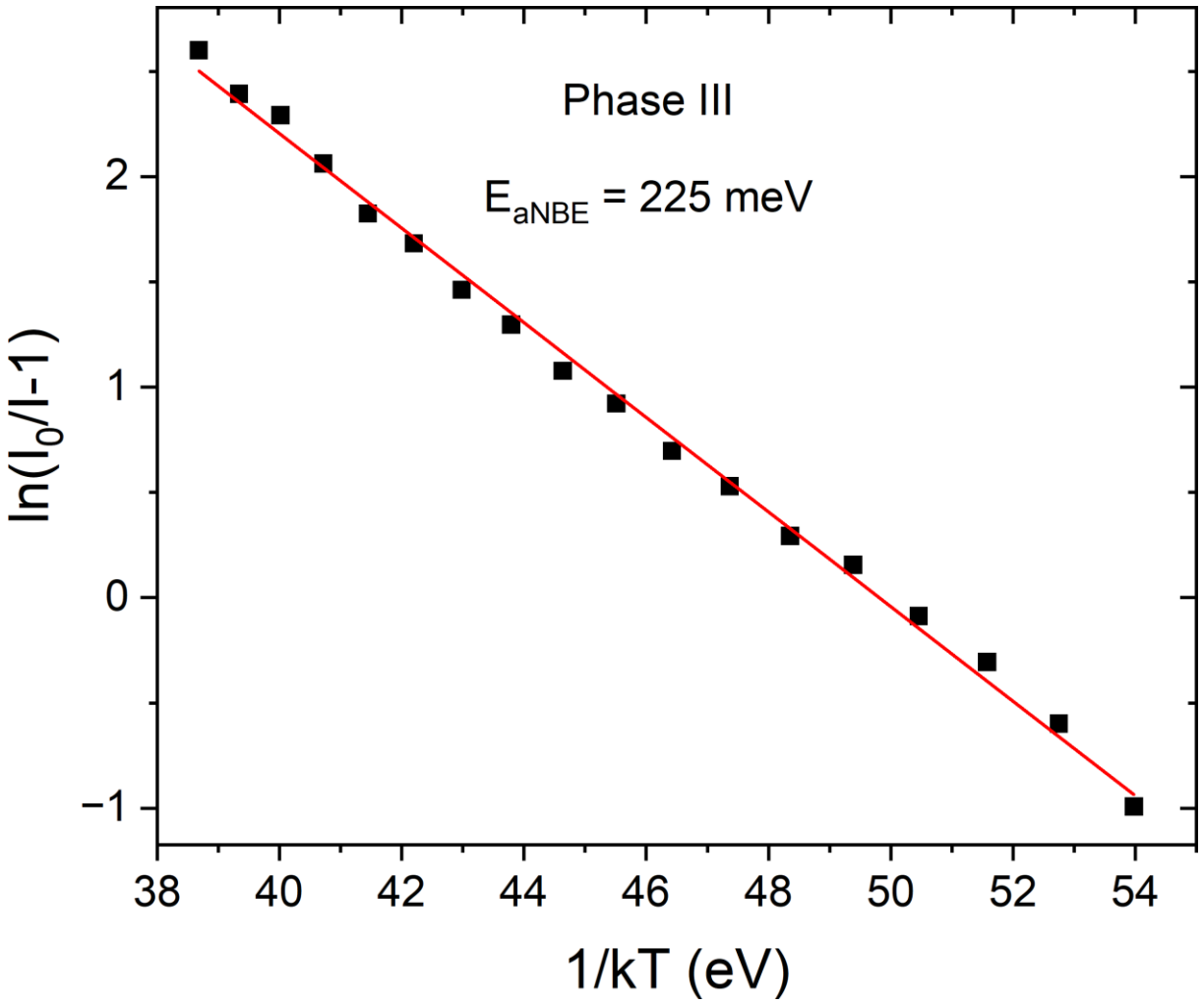

Figure S16. Logarithm of $I_0/I-1$ as a function of 1/kT of NBE emission of CPA_2PbBr_4 during cooling from 300 to 85 K. E_a was extracted by fitting the Arrhenius equation.

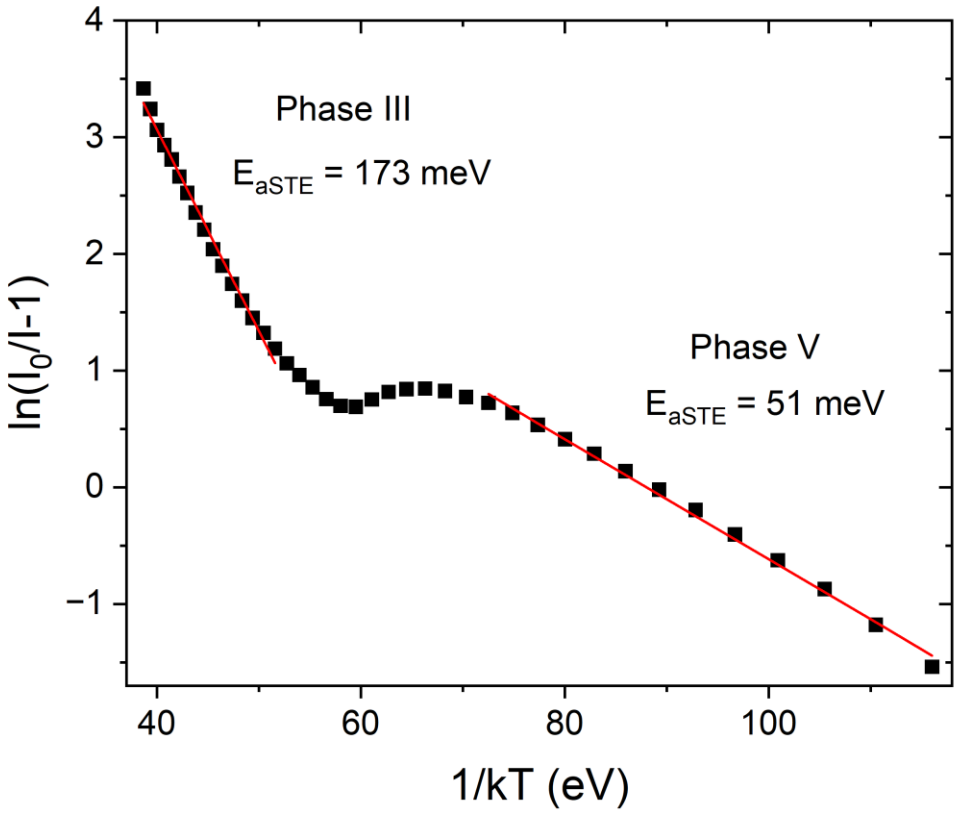

Figure S17. Logarithm of I_0/I-1 as a function of 1/kT of STE emission of annealed CPA_2PbBr_4 during cooling from 300 to 85 K. E_a was extracted by fitting the Arrhenius equation.

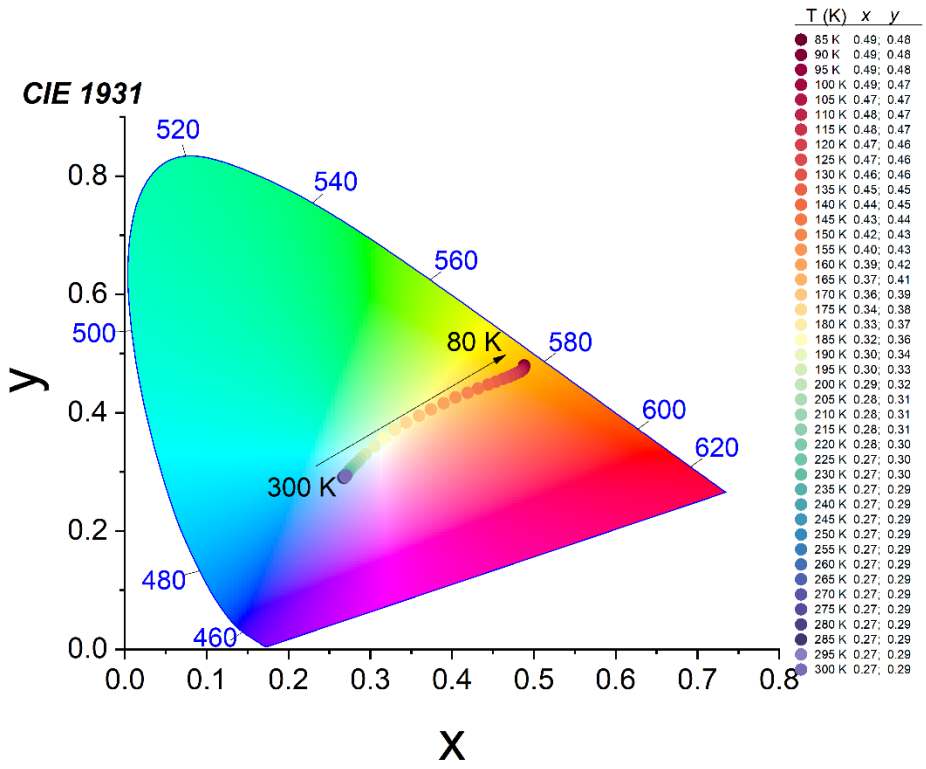

Figure S18. CIE coordinates of CPA_2PbBr_4 during cooling from 300 to 85 K.

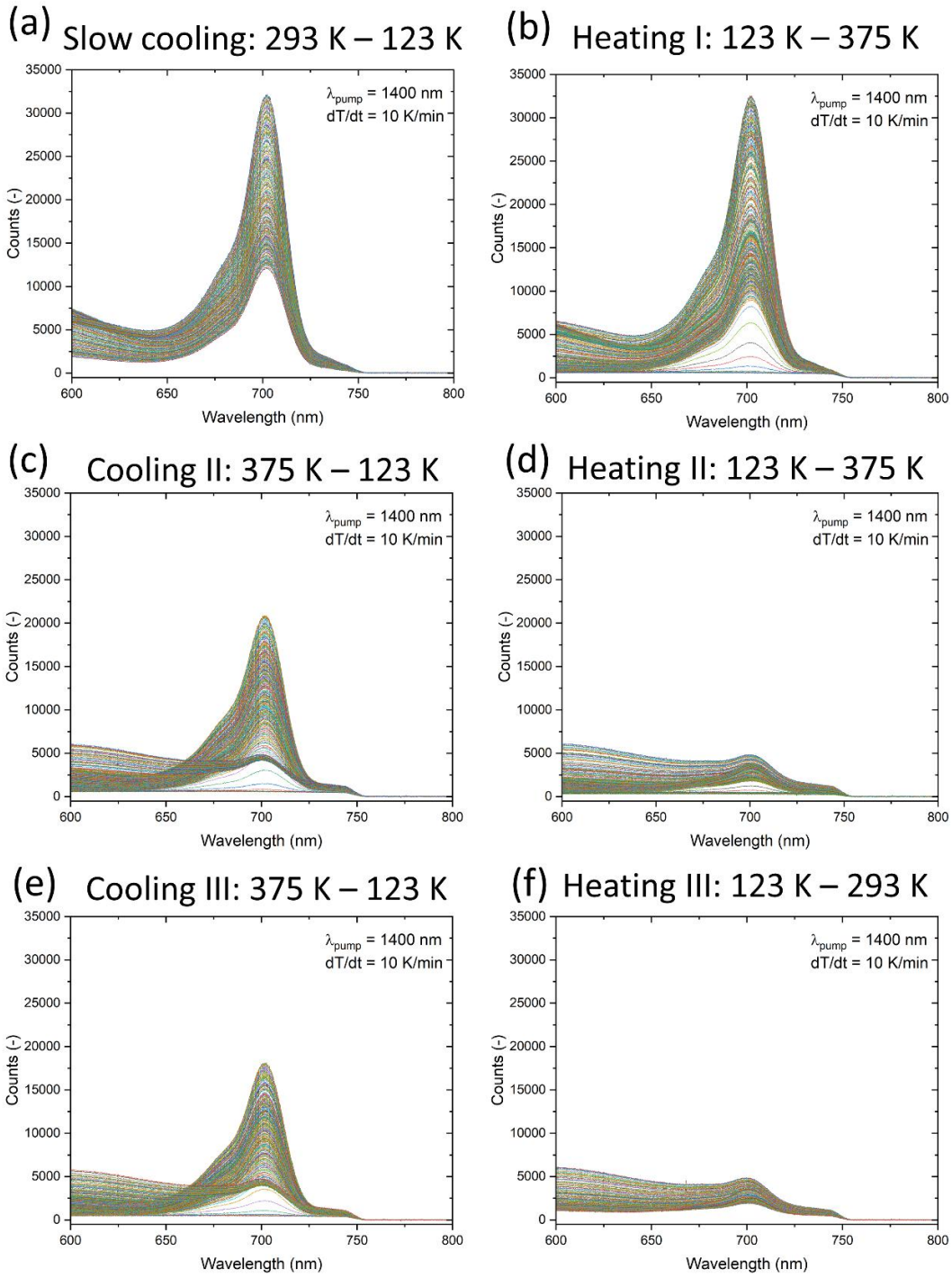

Figure S19. Temperature-resolved SHG spectra obtained for powdered CPA_2PbBr_4 sample during consecutive heating/cooling cycles: (a) slow cooling 293K – 123K, (b) heating I 123K – 375K, (c) cooling II 375K – 123K, (d) heating II 123K – 375K, (e) cooling III 375K – 123K, (f) heating III 123K – 293K.

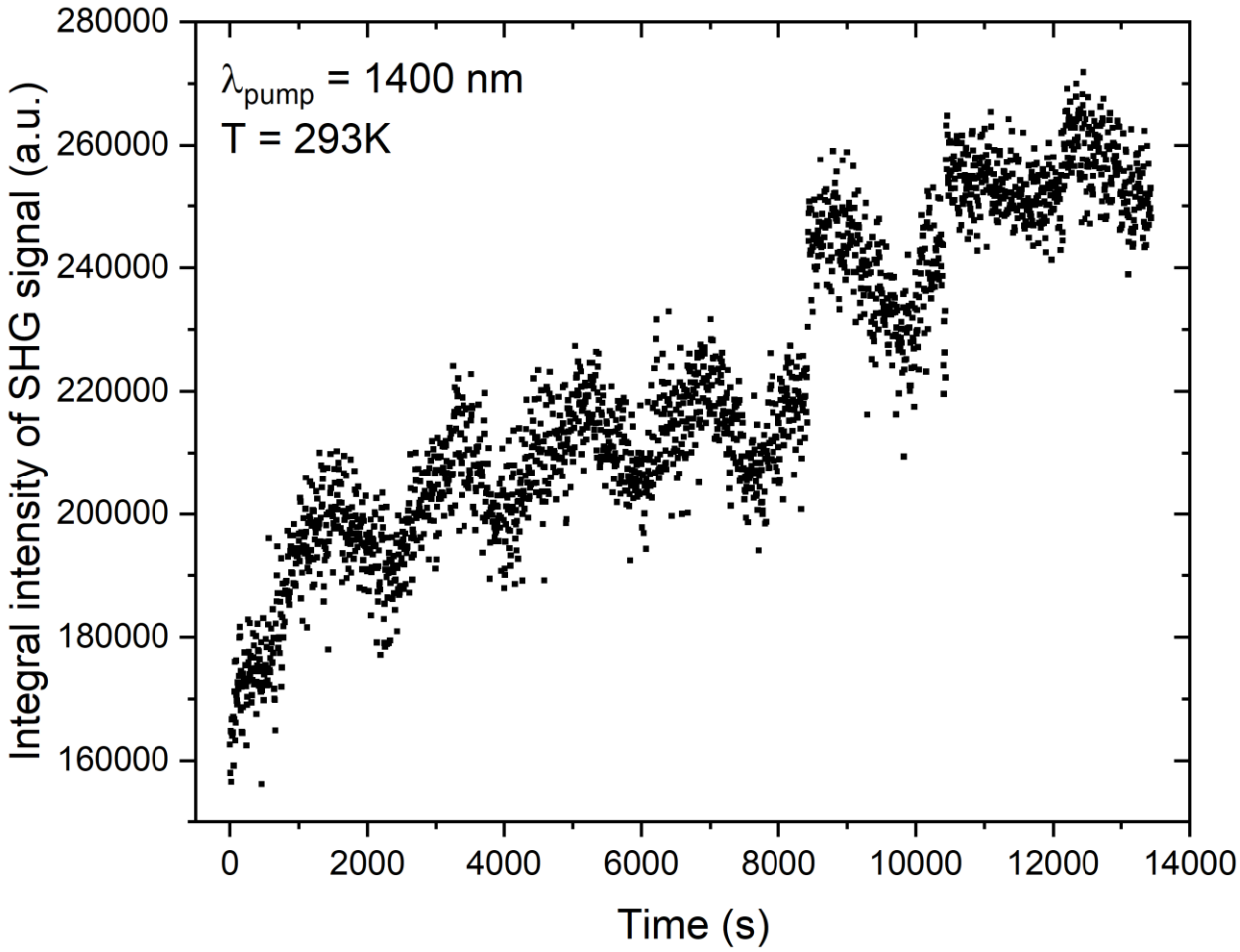

Figure S20. Plot of the integrated intensity of the SHG signal (λ_{SHG} = 700 nm) for a powdered CPA_2PbBr_4 sample that had previously been subjected to three heating–cooling cycles. Over the course of almost 4 hours, the SHG intensity increased by 68%. The sinusoidal component present in the SHG trace is due to intrinsic oscillations of the femtosecond laser used for the measurements.

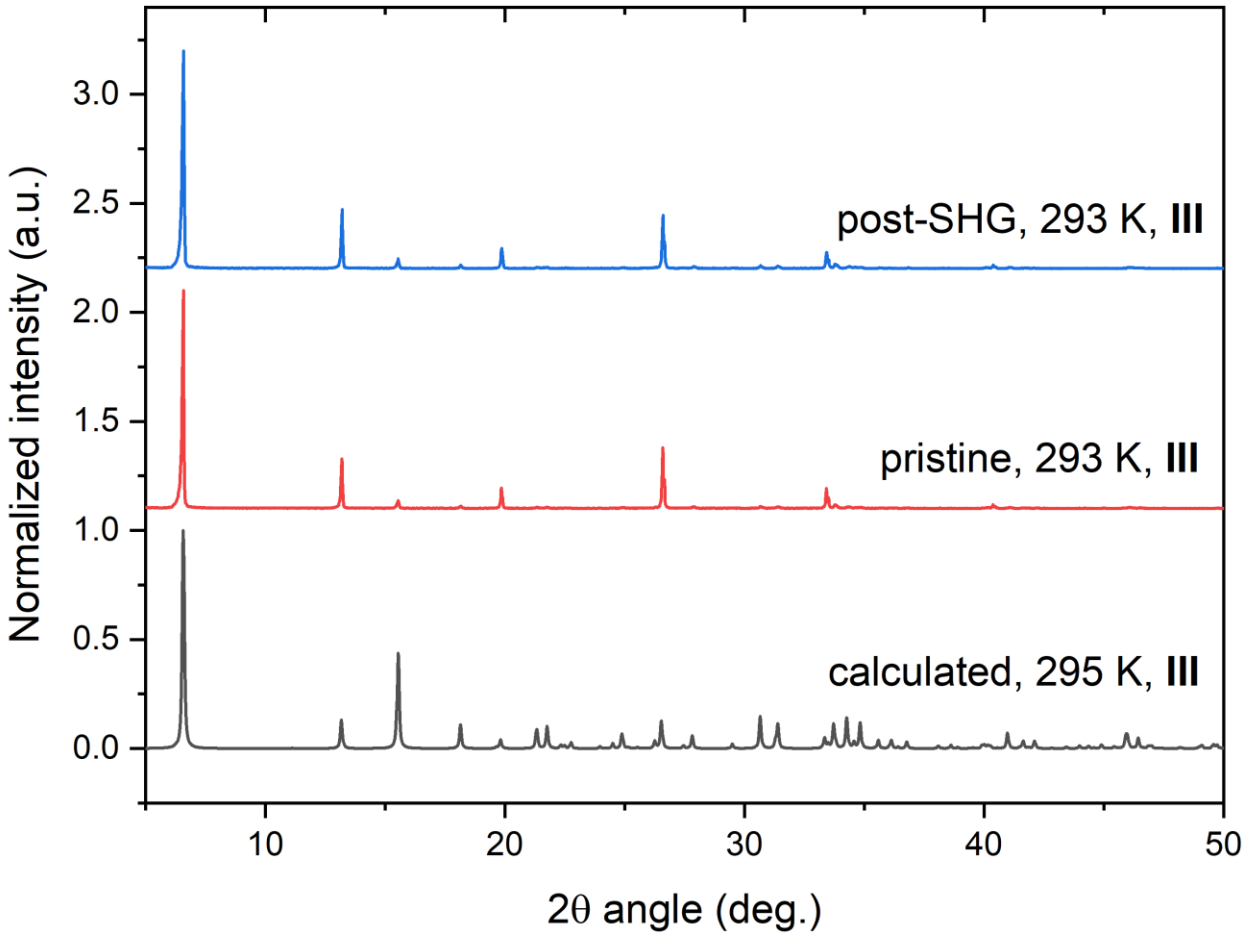

Figure S21. Theoretical PXRD pattern generated from the single-crystal structure (phase **III** of CPA_2PbBr_4), experimental PXRD pattern for pristine, powdered CPA_2PbBr_4 and experimental PXRD pattern for a powdered CPA_2PbBr_4 sample subjected to three heating–cooling cycles.

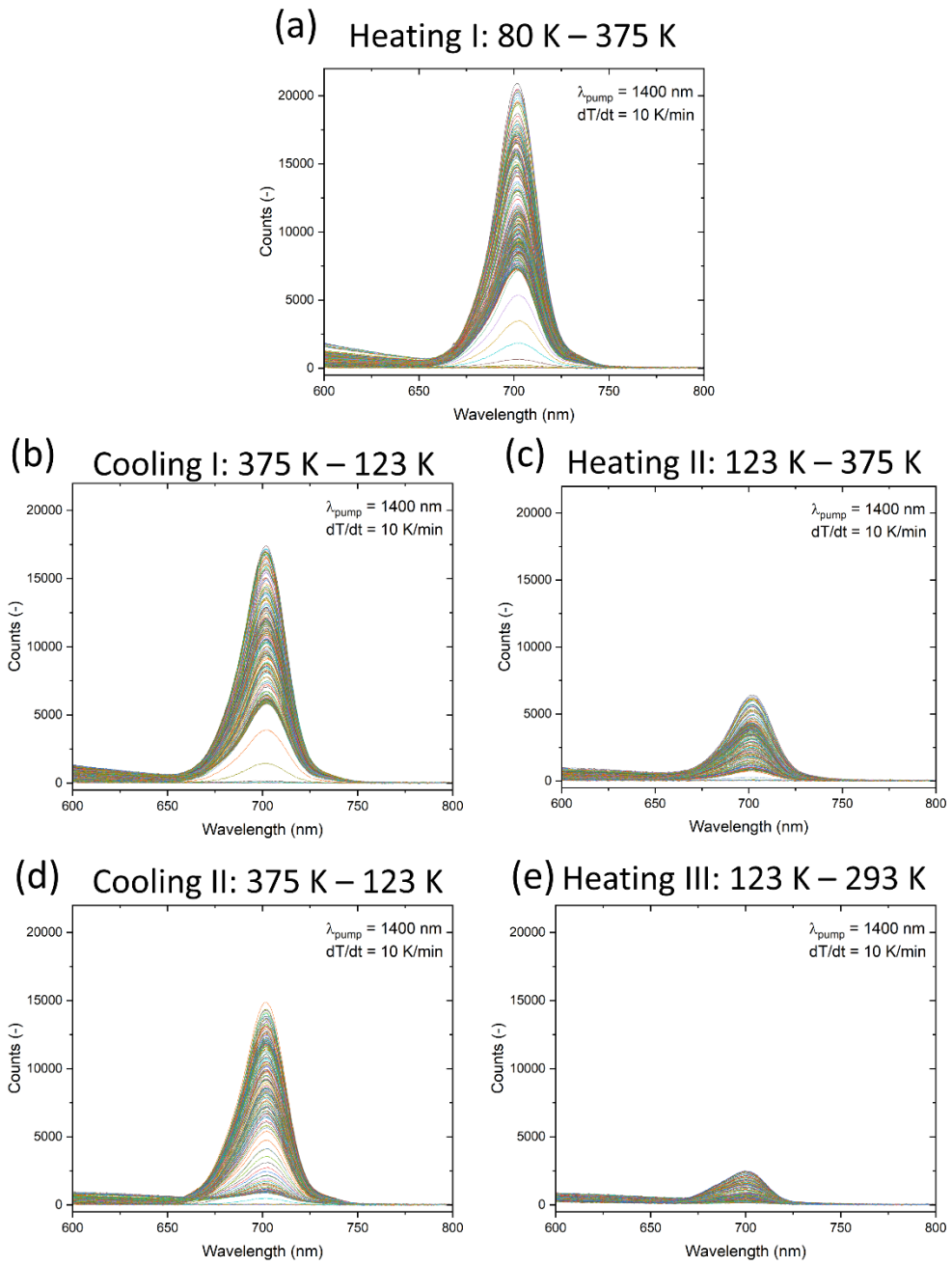

Figure S22. Temperature-resolved SHG spectra obtained for single crystal CPA_2PbBr_4 sample subjected to initial rapid cooling during consecutive heating/cooling cycles: (a) heating I 80K – 375K, (b) cooling I 375K – 123K, (c) heating II 123K – 375K, (d) cooling II 375K – 123K, (e) heating III 123K – 293K.

References

(1) M. D. Smith, A. Jaffe, E. R. Dohner, A. M. Lindenberg, H. I. Karunadasa, *Chem. Sci.,* 2017, **8**, 4497-4504.

(2) M. H. Jung, *Inorg. Chem*., 2019, **58**, 6748-6757.

(3) M. Mączka, J. K. Zaręba, A. Gągor, K. Fedoruk-Piskorska, D. Stefańska, D. Drozdowski, M. Ptak, A. Sieradzki, *ACS Appl. Mater. Interfaces*., 2024, **16**, 60564–60575.

(4) M. D. Smith, B. A. Connor, H. I. Karunadasa, *Chem. Rev.,* 2019, **119**, 3104–3139.